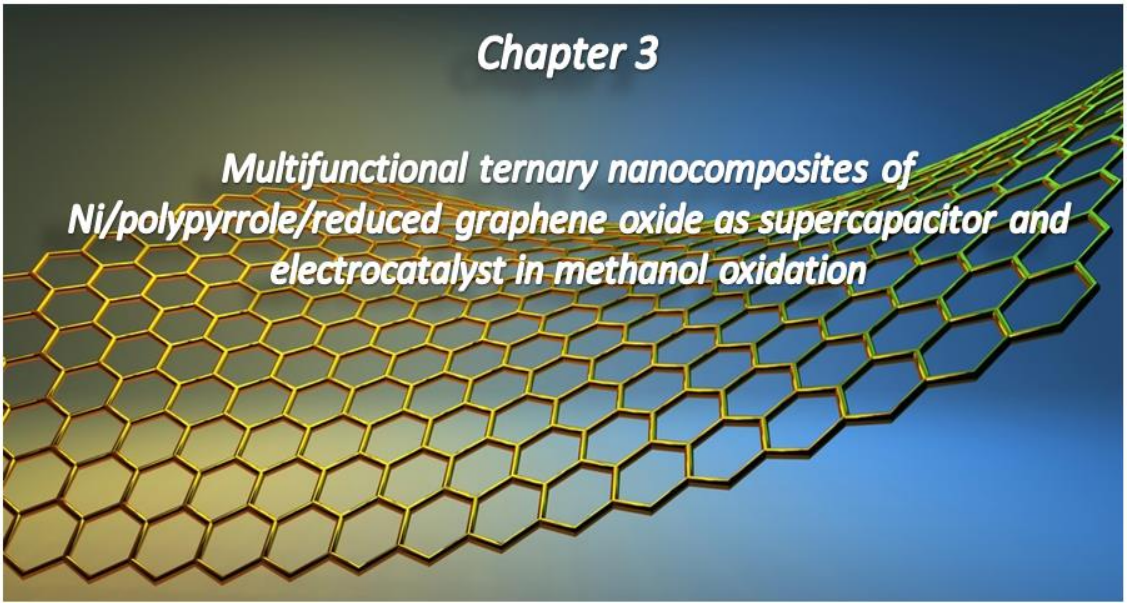

GRAPHICAL ABSTRACT

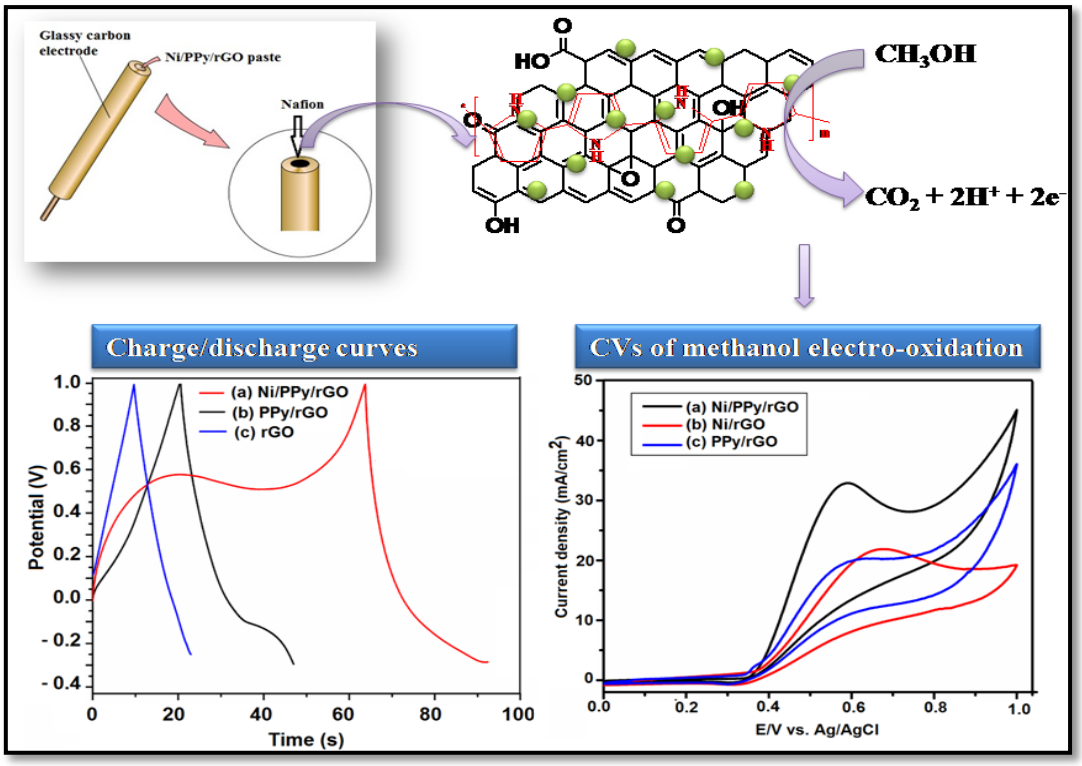

Ni/PPy/rGO acts as a multifunctional electrode material with high specific capacitance value of 763.49 Fg^{-1} at 1.31 Ag^{-1} and high electro-catalytic activity and stability towards methanol oxidation in alkaline medium.

3.1 Introduction

The rapid exhaustion of conventional fossil fuel reserves the increasing concern over environmental pollution has encouraged intensive research and development of new materials to improve the performance of advanced energy conversion and storage devices [1, 2]. The electrochemical energy production will be considered as an alternative energy/power source if energy consumption is designed to be of high-performance, low-cost and environmental friendly manner. System required for promising electrochemical energy storage and conversion include fuel cells, batteries and electrochemical capacitors [3]. Supercapacitors are gaining considerable interest because of their higher energy density and power density than batteries, faster charging time and more excellent cyclability [4, 5]. DMFCs have also recognized to be a promising power source for portable electronic devices and vehicles, due to the abundance of their raw materials, high efficiency and low emission [2, 6, 7]. It is necessary to develop multi-functional, low cost electrode materials which possess reasonably good performance to develop advanced supercapacitors and DMFCs.

Depending on the charge storage mechanisms supercapacitors are mainly classified into two broad categories. First category is electrical double layer capacitance (EDLC), which stores energy based on the reversible adsorption/desorption of ions that takes place at the interface between the electrode materials and the electrolyte. EDLC is based on carbonaceous materials that possess high power density but low capacitance. The carbonaceous materials have a common capacitance value of less than 40 μ F cm^{-2} of the real surface, which is an immense weakness for EDLC [8-10]. Another category is pseudocapacitor, a pseudocapacitor stores energy from rapid surface redox reactions that takes place on the surface and the near surface of the electrode materials. Pseudocapacitor based on metals, metal oxides or conducting polymers possesses high specific capacitance but due to low conductivity it suffers from poor cyclability [11]. The hybridization of EDLC and a pseudocapacitor can enhance the electrochemical performance [12, 13]. For example, Subramanium et al. [13] reported that amorphous MnO_2 single walled carbon nanotubes composites showed enhanced electrochemical

---

This part of the thesis is published in

Sarkar, C., Nath, J., Bhuyan, S., and Dolui, S. K. Chemistry Select, 4(9): 2529-2537, 2019.

properties both with respect to high rate capability and the discharged capacitance due to the inter-connection of MnO_2 and SWNTs.

DMFCs possess high energy density and easy solubility of raw materials compared to hydrogen fuel cells [14]. However, high manufacturing costs and slow rate of methanol oxidation reaction on the anode of the fuel cell have limited the commercialization of these fuel cells [15]. In order to overcome these problems a great deal of research has been carried out including detailed studies on Pt-based electro-catalysts in acidic medium [16-18]. But unfortunately, the commercialization of the Pt electrocatalyst is significantly hindered by the limited resource of Pt, high cost, low power density and poor CO-poisoning tolerance [19]. We are searching for a new low cost electrode for both the applications without compromising their properties.

Graphene sheets are ideal electrical double layer capacitor materials due to their high conductivity and good mechanical properties which are comparable to or better than carbon nanotubes [20]. In aqueous electrolyte solutions the specific capacitance values of graphene sheets as an electrode can achieve upto 135 F g^{-1}[21]. However, in aqueous electrolyte solutions they suffer from irreversible sheet-to-sheet restacking resulting in a limited accessibility to electrolyte ions hindering the full utilization of surfaces and active sites of graphene [22,23]. Graphene sheets also play an important role in the fabrication of advanced high performance composite electro-catalysts for DMFCs applications due to their extraordinary physiochemical properties [24-28]. They can provide enhanced mass transport owing to larger surface area of nanocatalyst for electron transfer [29, 30].

Graphene based nanocomposites can be combined with pseudocapacitive materials to enhance capacitance. The hybrid nanomaterials of pseudocapacitive materials and graphene can enhance the speed of electron through the supercapacitor electrode [31, 32]. For example, Zhang et al. synthesized graphene and polyaniline nanofibre nanocomposites that exhibited a high capacitance value of 480 F g^{-1} and cyclability compared to their individual counterparts [33]. Idris et al. prepared Ni/graphene for use as an electrode for supercapacitor (capacitance value 275 F g^{-1}) [34]. Ni nanoparticles supported on graphene composite was also utilized as electrode material for the DMFCs in alkaline medium [35]. Moreover, incorporating conducting polymers with high stability and high surface area has also been used to improve the activity of graphene based composites and enhanced the dispersing of metals [36, 37]. Among

various types of conducting polymers, polypyrrole (PPy) is mostly used in supercapacitor electrodes due to its various benefits such as good electrical conductivity, low cost, simple fabrication, easy of processing and good environmental stability. Graphene based PPy composites showed immense improvement in electrochemical behavior with diverse technological applications due to the synergetic effect.

In the present work, we have synthesized a ternary nanocomposite of Ni/polypyrrole/reduced graphene oxide electrode (Ni/PPy/rGO) via simply mixing PPy/rGO and $NiCl_2.6H_2O$ at pH 10.5, and investigated the physical and electro-chemical properties of Ni/PPy/rGO for its probable use as multi-functional electrode material in advanced energy devices. We have also studied the electro-chemical supercapacitive properties and elctro-catalytic performance for methanol electro-oxidation in alkaline medium.

3.2 Experimental section

3.2.1 Chemicals

Graphite powder (<20 micron) was purchased from Aldrich and used as received. Sodium nitrate ($NaNO_3$), potassium permanganate ($KMnO_4$), hydrogen peroxide (30% v/v), sodium hydroxide (NaOH), hydrazine monohydrate, nickel chloride hexahydrate, concentrated sulfuric acid (98%), hydrochloric acid, methanol, ethanol were obtained from Merck. Pyrrole monomer, ferric chloride, and nafion solution were purchased from Sigma-Aldrich and were used as received. Chloroform ($CHCl_3$) was procured from Merck and was distilled before use.

3.2.2 Synthesis of rGO and PPy/rGO composite

GO was synthesized from natural graphite powder by the modified Hummers method using $KMnO_4$ and H_2SO_4 as oxidizing agent [38]. The product was purified by washing with 5% HCl and then DI water for several times. The product was then exfoliated by ultrasonication for 1h to obtain the GO dispersion. GO dispersion was chemically converted to rGO using hydrazine monohydrate as a reducing agent at 80 °C.

PPy/rGO composites were prepared by liquid/liquid interfacial polymerization method involving pyrrole and rGO [39]. Where the aquous phase was prepared by dispersing 200 mg of rGO and 300 mg of $FeCl_3.6H_2O$ in 20 mL of water by

ultrasonication and the organic phase was prepared by dissolving 0.1 mL of pyrrole monomer in 20 mL of $CHCl_3$.

3.2.3 Synthesis of Ni/ PPy/rGO nanocomposites

Ni/PPy/rGO nanocomposite was synthesized simply by mixing PPy/rGO and $NiCl_2.6H_2O$ at pH 10.5. 100 mg of PPy/rGO was dispersed in 0.1 $molL^{-1}$ of $NiCl_2.6H_2O$ by ultrasonication. Then excess of $NaBH_4$ aqueous solution was added to the suspension under vigorous stirring until it reaches pH=10.5. Finally, the Ni/PPy/rGO nanocomposite was collected by filtration and thoroughly washing the product with warm DI water. The product was then dried at 50 °C and black coloured Ni/PPy/rGO powder was obtained.

For comparison, PPy and Ni/rGO nanocomposites were also synthesized. PPy was synthesized by interfacial polymerization of pyrrole in water/chloroform interface in presence of $FeCl_3.6H_2O$. Ni/rGO nanocomposites was synthesized from GO and $NiCl_2.6H_2O$ solution.

3.2.4 Characterization

The synthesized samples were characterized by FTIR, XRD, SEM, EDX and DLS method. The electrochemical properties of the samples were measured by using Bio Logic Science Instrument, SP-150 and power: 110-240 Vac voltammeter. X-ray photoelectron spectroscopy (XPS) was done using XPS Physical Electronics, PHI 5000, Versa Probe III instrument. Transmission Electron Microscopy (TEM) studied using 2100F (JEOL) FETEM instrument.

3.2.5 Electrochemical measurements

The electrochemical behavior of the prepare samples were studied using a standard one compartment three electrode system where Pt and Ag/AgCl electrodes were used as an counter and reference electrodes respectively. A glassy carbon electrode was used as the working electrode on which 1 µL of the catalyst paste was applied. The catalyst paste was prepared by dispersing 12.5 mg of the elctroccatalyst in 0.5 mL of ethanol by ultrasonication for 30 min. A measured volume of the paste was then pippeted onto the glassy carbon electrode. Then 5 wt% Nafion was added onto the paste and air dried for overnight. To measure the methanol electr-oxidation, CV was performed between 0.0 V to 1.0 V at a scan rate of 50 mVs^{-1} in 1 M KOH containing 1 M methanol.

The chonoamperometry was performed to measure the stability of the electrocatalyst for 600 s at a fixed potential of 0.4 V.

3.3 Results and discussion

3.3.1 FTIR analysis

FTIR spectra of GO, rGO, PPy, PPy/rGO and Ni/PPy/rGO are shown in Fig. 3.1. In the FTIR spectrum of GO (Fig. 3.1a), the peaks obtained at 1265, 1068 and 1720 cm^{-1} are attributed to the C-O epoxy stretching, C-O alkoxy stretching and C=O carbonyl stretching vibrations, respectively. The absorption peaks at 1621 and 3426 cm^{-1} correspond to the aromatic C=C stretching vibration and O-H stretching vibration, respectively. After reduction of GO, the characteristic peak of C=O stretching vibration of carboxyl at 1720 cm^{-1} disappeared completely for rGO (Fig. 3.1b). Also, peak intensity corresponds to C-O epoxy and C-O alkoxy stretching vibration decreases significantly. The absorption peaks due to aromatic C=C stretching vibration and O-H stretching vibration shifted from 1621 cm^{-1} to 1556 cm^{-1} and 3426 cm^{-1} 3413 cm^{-1}, respectively. These results confirm that GO was successfully reduced to rGO. In the FTIR spectra of PPy (Fig. 3.1), peaks at 1461, 1536, and 3433 cm^{-1} associated with the C-N, C-C, and N-H stretching vibration of pyrrole ring [40, 41]. The peaks at 2924 cm^{-1} and 2851 cm^{-1} are designated as the asymmetric and symmetric stretching vibrations of CH_2 of PPy [42]. In the spectrum of PPy/rGO nanocomposites (Fig. 3.1d), it can be observed that all characteristic peaks of PPy are present with little shifting which is probably due to the π-π interaction between the rGO layers and PPy rings. The characteristics peaks of PPy are shifted from 1461, 1536, and 3433 cm^{-1} to 1454, 1547, and 3426 cm^{-1} in the FTIR spectrum of PPy/rGO. Moreover, the peak due to epoxide group and C=C stretching vibrations of rGO are appeared at 1271 and 1629 cm^{-1} respectively, in the FTIR spectra of PPy/rGO. Thus FTIR analysis confirms the presence of PPy and rGO in the PPy/rGO composite as well as successful combination of both the components. Generally, metal does not any characteristic peaks in FTIR spectrum [43]. In the FTIR spectra of Ni/PPy/rGO, there is a considerable shift of characteristic peaks PPy and rGO. This is because of the presence of metallic Ni over PPy/rGO. Thus, FTIR results confirm the successful formation of Ni/PPy/rGO nanocomposites.

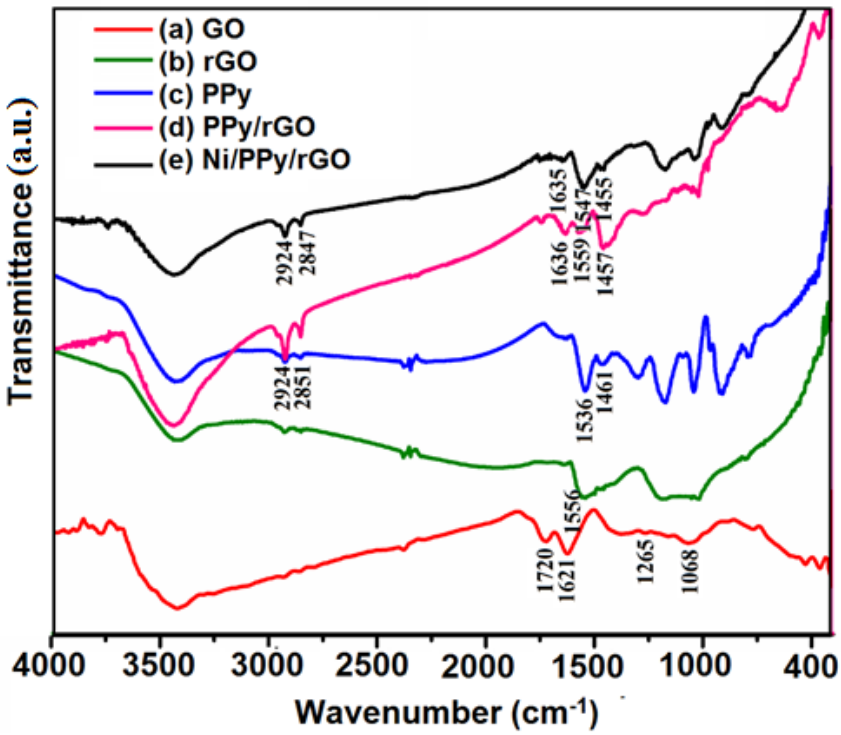

Fig. 3.1 FTIR spectra of (a) GO (b) rGO (c) PPy (d) PPy/rGO (e) Ni/PPy/rGO

3.3.2 XRD analysis

The structure of the synthesized composites was investigated by XRD analysis. Fig. 3.2 shows the XRD patterns of GO, rGO, PPy/rGO and Ni/PPy/rGO nanocomposites. The pristine graphite shows a very strong peak at 2θ=26.5° for the (002) plane while the GO shows a broad peak at 2θ=12.5°, (Fig. 3.2a) corresponds to (002) plane indicating oxidation of pristine graphite. After reduction, two new broad peaks are observed at 2θ=25.45° and at 2θ=42.8° (Fig. 3.2b) corresponds to the loosely stack graphene sheets. In the XRD pattern of PPy/rGO composite shifting of the peak is observed (Fig. 3.2c). The peak at 2θ=25.45° has been shifted to 26.3° which is due to the π-π interaction between PPy and rGO sheets. In the XRD pattern of NI/PPy/rGO nanocomposites (Fig. 3.2d), two new sharp diffraction peaks are observed at 2θ=43.9° and 2θ=52.7° which corresponds to the (111) and (200) planes of cubic face centered structure of Ni (JCPDS card no. 65-2865), indicating formation of Ni after reduction process. Thus the XRD results indicate successful incorporation of metallic Ni in the PPy/rGO matrix.

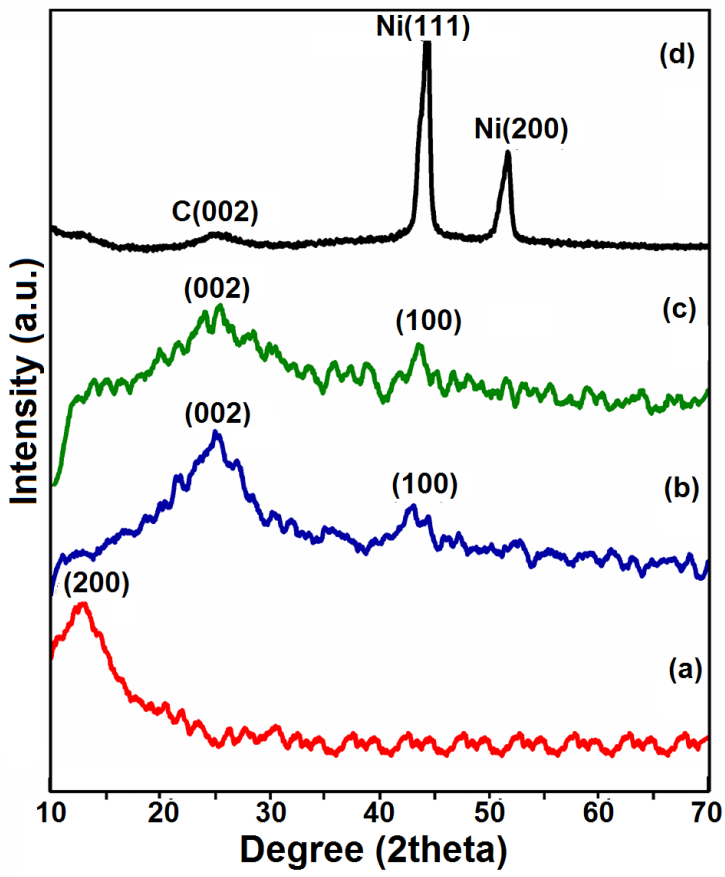

Fig. 3.2 XRD pattern of (a) GO (b) rGO (c) PPy/rGO and (d) Ni/PPy/rGO

3.3.3 Raman analysis

Since Raman spectroscopy is useful for studying disorder and defects in crystal structure, it is often employed to characterize carboneous materials. The Raman spectra for the GO, PPy, PPy/rGO, and Ni/PPy/rGO nanocomposites are shown in Fig. 3.3. The D band in Raman spectra is related to the defects and disorder in the hexagonal lattice, while the G band in Raman spectra corresponds to an E_{2g} mode of graphite which is related to the vibration the sp^2-bonded carbon atom in the hexagonal lattice. Therefore, the intensity ratio between the disorder induced D band and the G band (I_D/I_G) states the atomic ratio of sp^2/sp^3 carbons which measures the extent of disorder graphite. The G bands are seen at 1603 cm^{-1}, 1581 cm^{-1}, 1598 cm^{-1}, and 1596 cm^{-1} and the D bands are at 1360 cm^{-1}, 1380 cm^{-1}, 1353 cm^{-1}, and 1356 cm^{-1}, for GO, PPy, PPy/rGO and Ni/PPy/rGP, respectively. The calculated I_D/I_G ratio for GO is 0.88 which indicates high level of disorder of the GO layers due to the presence of oxygen functional groups on graphite. For, the pure PPy, the D and G bands are attributed to the ring stretching and C=C backbone stretching mode of PPy, respectively [44]. In addition, the three bands

appeared at 1051 cm^{-1}, 975 cm^{-1}, and 932 cm^{-1}, are related to the in-plane and out-of-plane vibrations of N-H and C-H modes of PPy [45, 46]. PPy/rGO and Ni/PPy/rGO nanocomposite shows the bands of PPy which proofs the presence of PPy in the composites. Moreover, the decrease of the I_D/I_G values for PPy/rGO (0.84) and Ni/PPy/rGO (0.82) showed that the disordered of rGO is lesser.

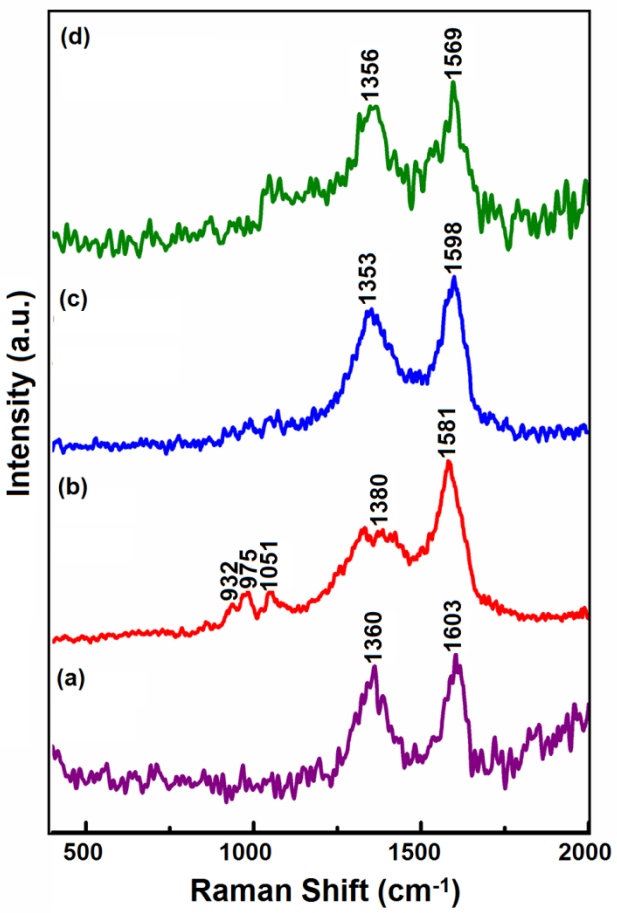

Fig. 3.3 Raman spectra of (a) GO (b) PPy (c) PPy/rGO and (d) Ni/PPy/rGO

3.3.4 SEM and EDX analysis

The structural analysis of the rGO, PPY, PPy/rGO, and Ni/PPY/rGO were investigated using scanning electron microscope (SEM). The SEM image of rGO shows a layered, wrinkled-like structure (Fig. 3.4a). The pure PPy exhibits sphere-like structure (Fig. 3.4b). In the SEM image of PPy/rGO (Fig. 3.4c), the sphere like structure of PPy is disappeared and wrinkled, multilayered structure corresponds to rGO sheets is observed. This change in the structure of the PPy/rGO composite is due to the polymerization of PPy on the rGO surface. In the SEM image of Ni/PPy/rGO, over wrinkled structure of PPy/rGO some nanoparticles are observed (Fig. 3.4d). This indicates that Ni

nanoparticles are uniformly deposited on the crumpled surface of the PPy/rGO. In addition, the presence of elemental Ni, C and O is confirmed from EDX spectrum (Fig. 3.5).

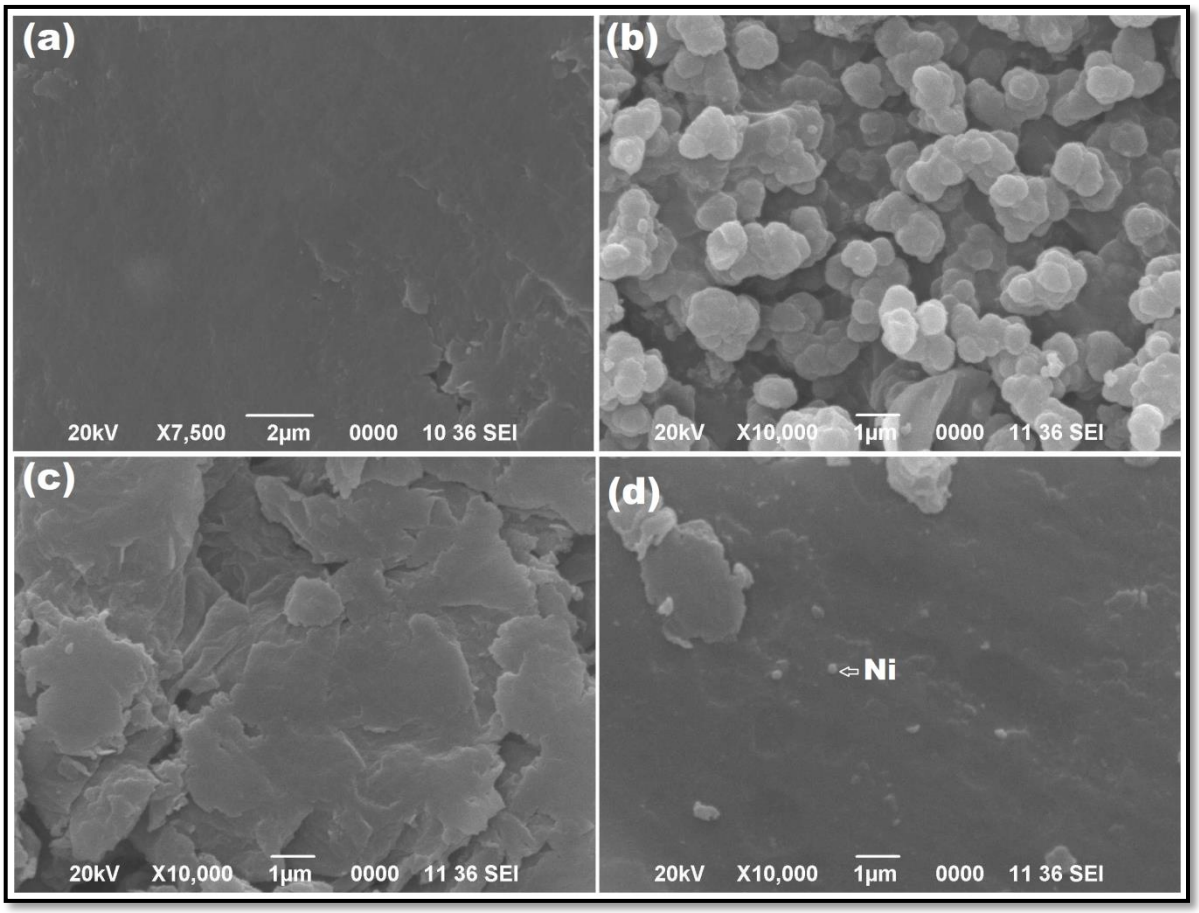

Fig. 3.4 SEM images of (a) GO (b) PPy (c) PPy/rGO and (d) Ni/PPy/rGO nanocomposites

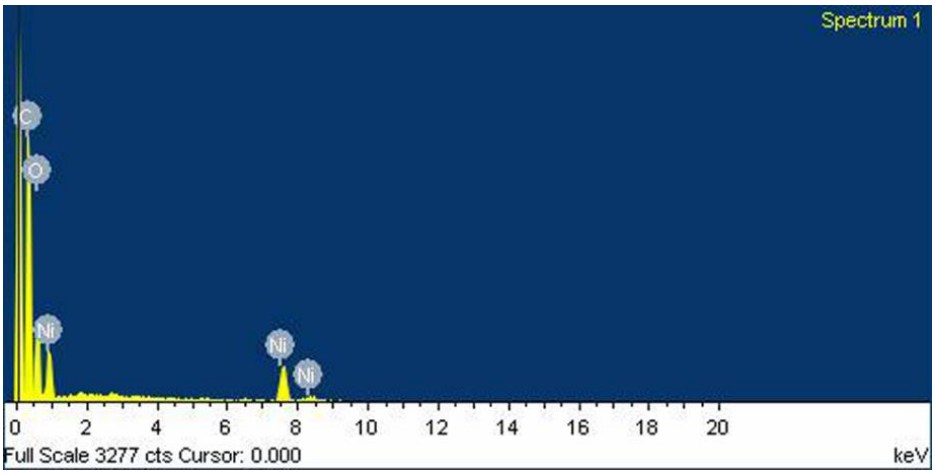

Fig. 3.5 EDX analysis of Ni/PPy/rGO nanocomposites

3.3.5 TEM and XPS analysis

TEM image of Ni/PPy/rGO nanocomposite is shown in Fig. 3.6a. TEM image indicates that the Ni nanoparticles are dispersed above the surface of PPy/rGO. Fig. 3.6b shows the XPS survey spectra of Ni/PPy/rGO nanocomposite. The survey spectrum also presented the presence of C, O, N and Ni in Ni/PPy/rGO nanocomposite.

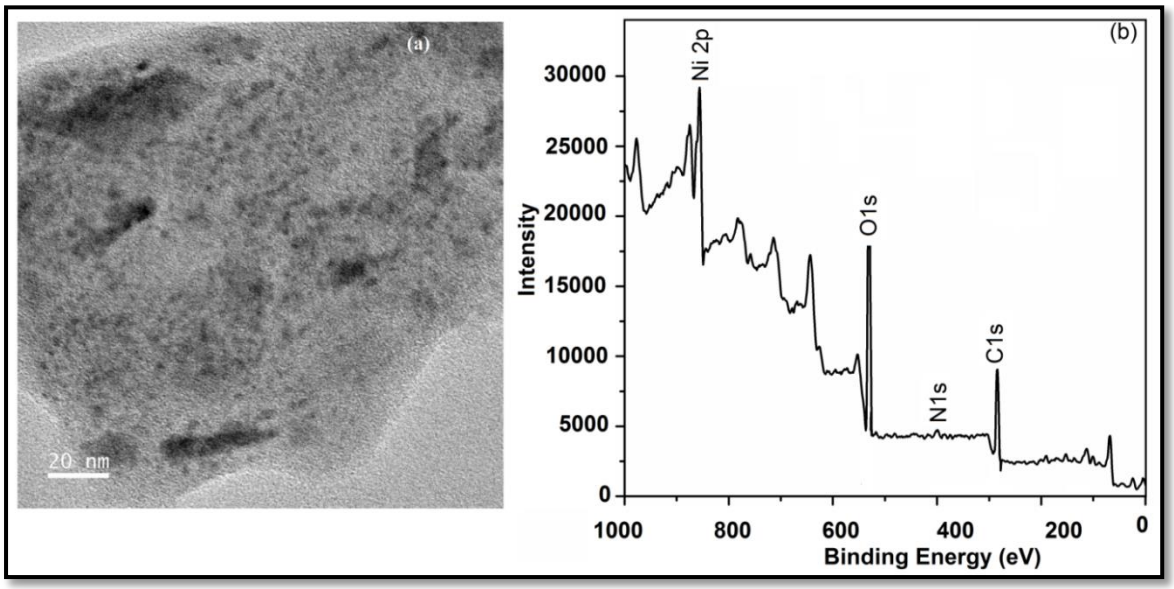

Fig. 3.6 (a) TEM and (b) XPS analysis of Ni/PPy/rGO nanocomposites

3.3.6 Particle size distribution

Particle size distribution of Ni/PPy/rGO nanocomposites is shown in Fig. 3.7. The diameter of the nanocomposite ranged from 0.97 nm to 1.23 nm and the mean diameter is 1.05 nm.

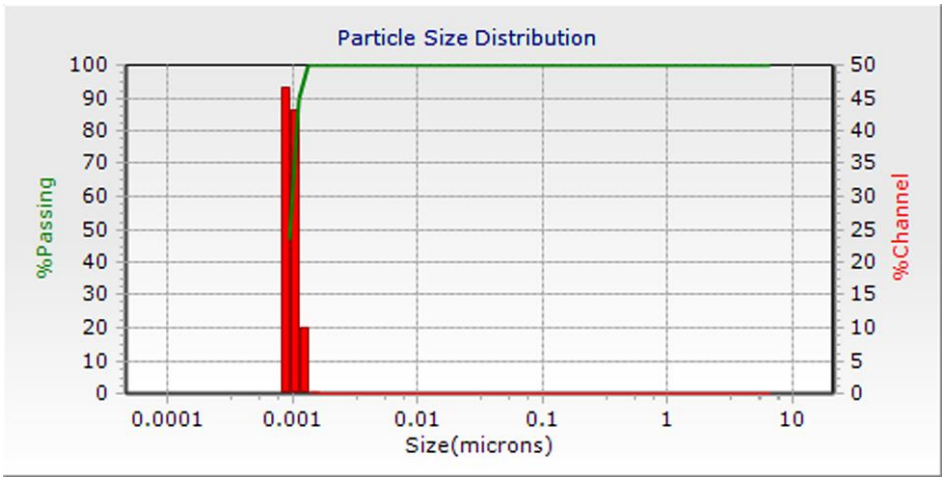

Fig. 3.7 Particle size distribution of Ni/PPy/rGO nanocomposites

3.3.7 Electrochemical studies

3.3.7.1 Cyclic Voltammetry (CV) studies

CV measurements were conducted in a three-electrode system using 1 M KOH solution as an electrolyte. Fig. 3.8 illustrates the CV of rGO, PPy/rGO, and Ni/PPy/rGO nanocomposite electrode with a potential range from -1.0 to 1.0 V at 20 mVs^{-1} scan rate. Both rGO and PPy show rectangular CV curve which is due to EDLC of rGO. However, the CV curve of Ni/rGO produces a pair of redox corresponds to $Ni(OH)_2$/NiOOH surface redox couple (equation 2) due to the Faradaic reactions (fig.3.8d inset) [47, 48]. Two well defined peaks are observed: one is the anodic peak i.e. the oxidation peak in the forward scan which corresponds to oxidation of Ni^{2+} to Ni^{3+} and the other is the cathodic peak i.e. the reduction peak which corresponds to reduction of Ni^{3+} to Ni^{2+} . The reactions are:

$$Ni + 2OH^- \longrightarrow Ni(OH)_2 + 2e \quad (1)$$

$$Ni(OH)_2 + OH^- \rightleftharpoons NiOOH + H_2O + e \quad (2)$$

CV curve of the Ni/PPy/rGO nanocomposite demonstrates nearly rectangular form with a larger area, indicating ideal capacitive nature and superior charge transport than that of rGO and PPy/rGO (Fig. 3.8a). The interaction between Ni nanoparticles PPy and rGO produces a better electrochemical performance because of the pseudocapacitance arising from Ni and PPy and the EDLC contribution by the rGO.

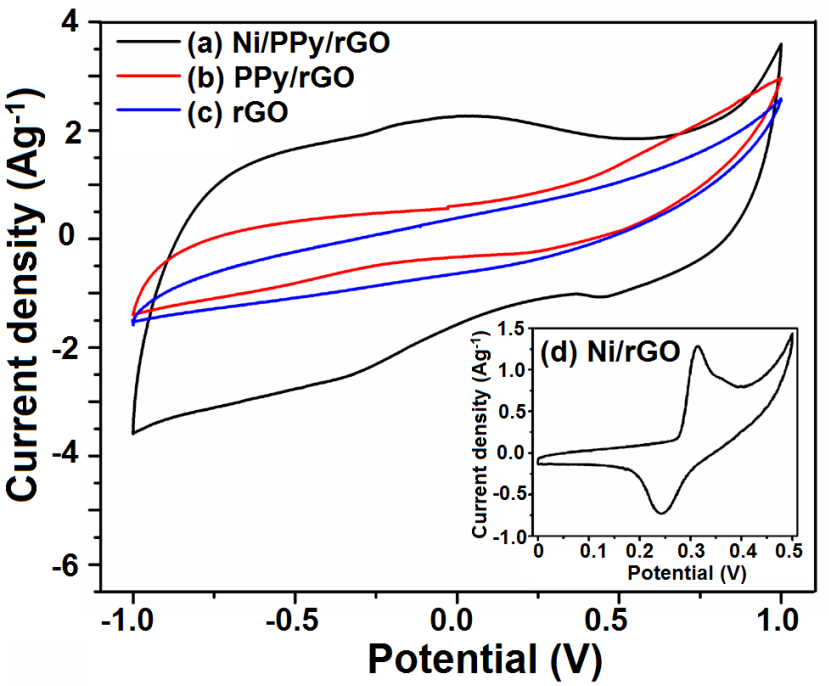

Fig. 3.8 Cyclic voltammograms of (a) Ni/PPy/rGO (b) PPy/rGO (c) rGO and (d) Ni/rGO (inset)

Fig. 3.9a illustrates CV of the Ni/PPy/rGO nanocomposites electrode at various scan rates from 2 to 100 mVs^{-1}. The outline of the CV curves is rectangular in shape, even at 100 mVs^{-1}, revealing great capacitance and good ion response of the nanocomposite. In addition, the voltammetric current is directly proportional to the scan rate as expected for an ideal capacitive behavior. To study the stability of the nanocomposites, CV was conducted for 200 continuous cycles at 100 mVs^{-1} scan rate. Fig. 3.9b shows that after repetitive 200 cycles, Ni/PPy/rGO still retained its electroactivity indicating an excellent high rate performance.

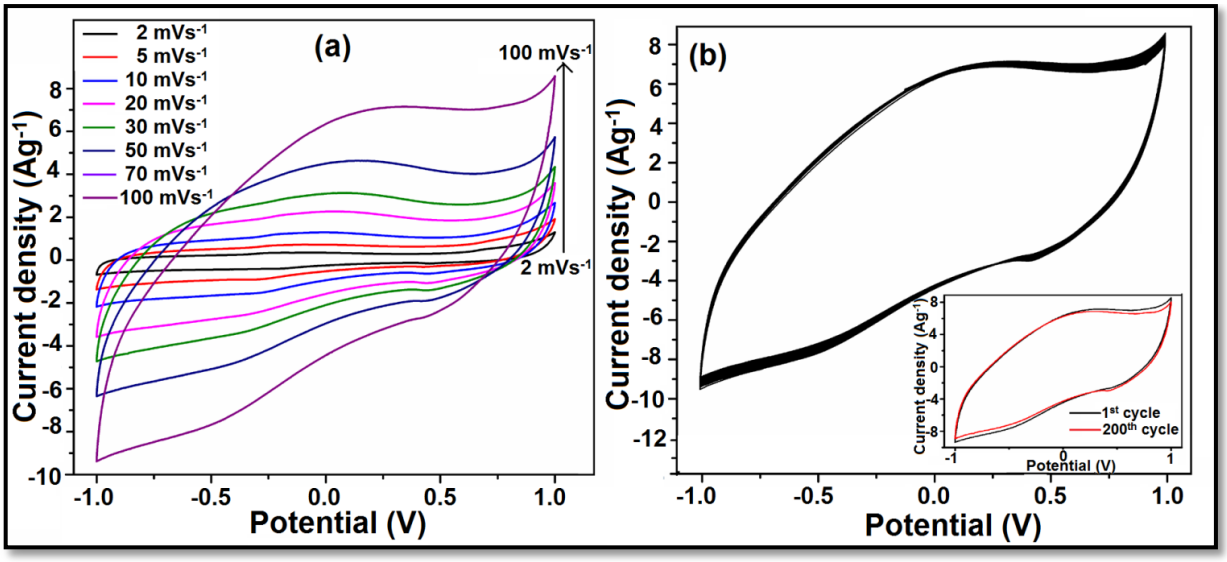

Fig. 3.9 (a) CVs recorded at different scan rate and (b) CVs for continuous 200 cycles for Ni/PPy/rGO

3.3.7.2 Galvanostatic Charge-Discharge Study

To study the charge capacity of the samples, the galvanostatic charge-discharge (GCD) measurements were also carried out. On the basis of the GCD study, the specific capacitance (C_s) of the electrode can be calculated using the following equation:

$$C_s = I\,\Delta t / m\,\Delta V \qquad (3)$$

Where, I, Δt, m and ΔV are the response current, discharge time, active mass and open potential, respectively. Figure 10a exhibits a set of CD curves for the Ni/PPy/rGO at different current densities. Fig. 3.10b illustrates the relationship between current density and C_s. The C_s value of Ni/PPy/rGO is 763.29 Fg^{-1} 1.31 Ag^{-1} current densities. On increasing current density from 1.31 to 30.85 Ag^{-1}, the C_s value decreases from 763.49 to 38.39 Fg^{-1}. The decrease in the C_s values with increasing current densities is because of the redox reaction that occurs at the electrode/electrolyte interface. These C_s values are in good agreement with the results that were obtained from the CV tests at different scan rates (Fig. 3.10a). In addition, the Ni/PPy/rGO nanocomposite retains 96.75% over 200 cycles at a current density 9.37 Ag^{-1} (Fig. 3.10c) indicating EDLC and pseudocapacitance materials.

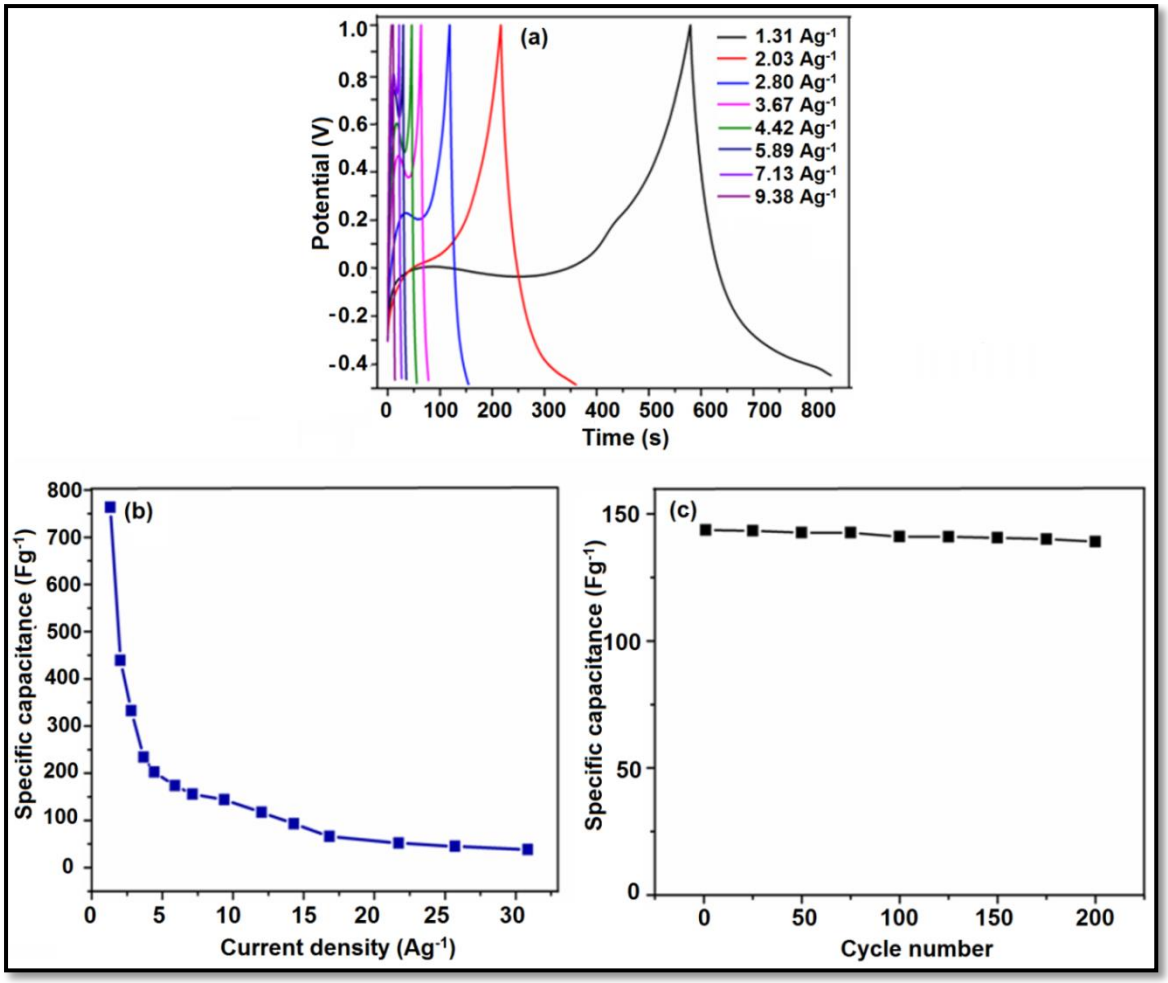

Fig. 3.10 (a) Charge/discharge curves of Ni/PPy/rGO at different current densities (b) Specific capacitances of Ni/PPy/rGO at different current densities and (c) Cyclic stability of Ni/PPy/rGO upto 200 charge/discharge cycles (current density 9.37 Ag^{-1}).

Fig. 3.11 shows the GCD curves of rGO, PPy/rGO and Ni/PPy/rGO at a current density 3.67 Ag^{-1} with potential range between -1.0 to 1.0 V. The triangular shape of charge/discharge curve of rGO indicates pure EDL capacitance. The shape of the measured CD curve of Ni/PPy/rGO is not an ideal straight line. The observed capacitive behavior of the nanocomposite is a result of the EDL and the pseudocapacitances of rGO, Ni and PPy. Also, the Ni/PPy/rGO nanocomposite shows longer discharge time compared to rGO and PPy/rGO at same current density. The C_s value of Ni/PPy/rGO is much higher (234.25 Fg^{-1}) than that of (76.68 Fg^{-1}) and rGO (35.53 Fg^{-1}) at 3.67 Ag^{-1} current density. The C_s value of Ni/PPy/rGO is also much higher than rGO/Ni foam composite (maximum C_s value 323 $mFcm^{-1}$ at 0.5 $mAcm^{-2}$) reported by Zhoong-Zhen Yu et.al [49] The increased C_s value is due to the synergetic effect of Ni, PPy and rGO.

Thus, the presence of PPy significantly increases the electrochemical properties of Ni/PPy/rGO nanocomposites.

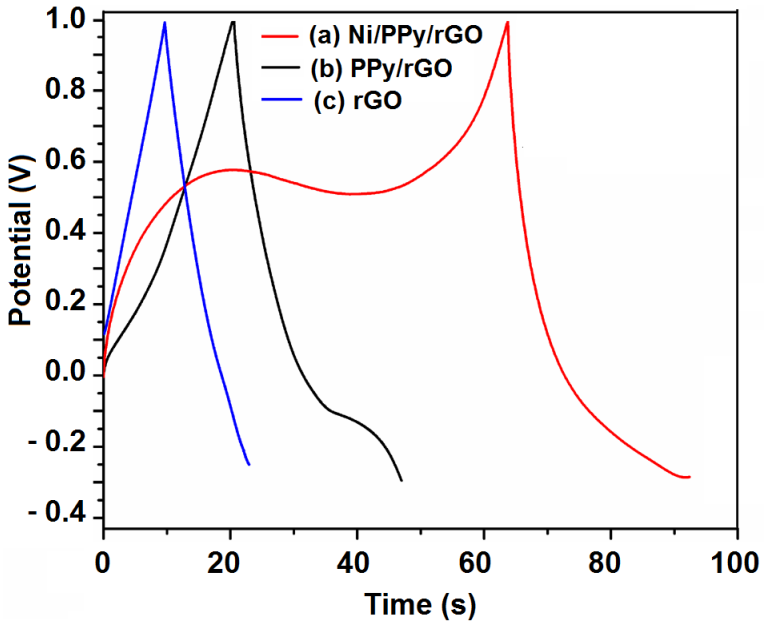

Fig. 3.11 Charge/discharge curves of (a) Ni/PPy/rGO, (b) PPy/rGO and (c) rGO (current density 3.67 Ag^{-1}).

3.3.7.3 Electrochemical Impedance Spectroscopy Study (EIS)

Electrochemical impedance spectroscopy studies were carried out in the frequency range from 10^5 Hz to 10 Hz. Fig. 3.12 shows the Nyquist plot for the PPy/rGO and Ni/PPy/rGO. Both the impedance curves of PPy/rGO and Ni/PPy/rGO intersects the *x*-axis at 45° angle in the beginning, suggesting typical feature of a porous electrode. The equivalent electrical circuit is shown in the inset of Fig. 3.12. The *x*-intercept of the curves in the high frequency region of the Nyquist plot represents the equivalent series resistance (Rs). Rs values of PPy/rGO and Ni/PPy/rGO are 9.72 and 4.72 Ohm, respectively. The lower Rs value for Ni/PPy/rGO nanocomposite indicates more conductive nature of the nanocomposite. The semicircle observed at higher frequency region of the plot refers to the interfacial charge-transfer resistance (Rct). Rct values of PPy/rGO and Ni/PPy/rGO are 32.8 and 5.39 Ohm, respectively. In the low-frequency region the 45° slope of the nearly vertical line indicates the Warburg resistance (Wd) representing good capacitance and low diffusion resistance of the composite. Thus, EIS results show that the Ni/PPy/rGO nanocomposite possesses efficient charge transfer and better capacitive nature than that of PPy/rGO.

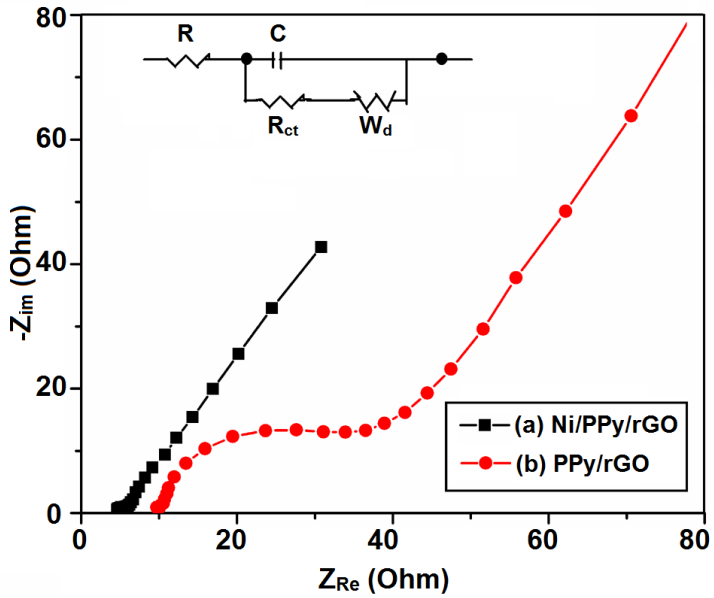

Fig. 3.12 Nyquist impedance plots of (a) Ni/PPy/rGO and (b) PPy/rGO

3.3.7.4 Electrocatalytic oxidation of methanol

Until now, we have presented the electrochemical energy storage properties of the Ni/PPy/rGO nanocomposites. To reveal its use in another energy device application, CV and chronoamperometry analysis were conducted to investigate their properties as electro-catalyst towards methanol electro-oxidation. Fig. 3.13 illustrates the CVs of Ni/PPy/rGO, Ni/rGO and PPy/rGO recorded in 1.0 M methanol solution containing 1M KOH at a scan rate of 50 mVs^{-1} in potential range of 0.00 to 1.00 V at room temperature. Fig. 3.13 clearly indicates a very well defined anodic peak in the forward scan which is due to the oxidation of freshly chemisorbed species from methanol adsorption while its corresponding cathodic peak diminishes notably, demonstrating thereby the electro-oxidation of methanol. These results demonstrate that the entire Ni^{3+} species are reduced to Ni^{2+} species through oxidation with methanol and almost no Ni^{3+} species are left for reduction to Ni^{2+}. These results support the findings of Fleischmann et al. that Ni^{3+} acts as an electrocatalyst towards electro-oxidation of alcohols in alkaline medium and alcohols get oxidized at a potential which coincide exactly with that where Ni^{3+} was produced [50, 51]. Thus, these results illustrate that methanol oxidation takes place on the Ni^{3+} surface where Ni^{3+} works as an electrocatalyst.

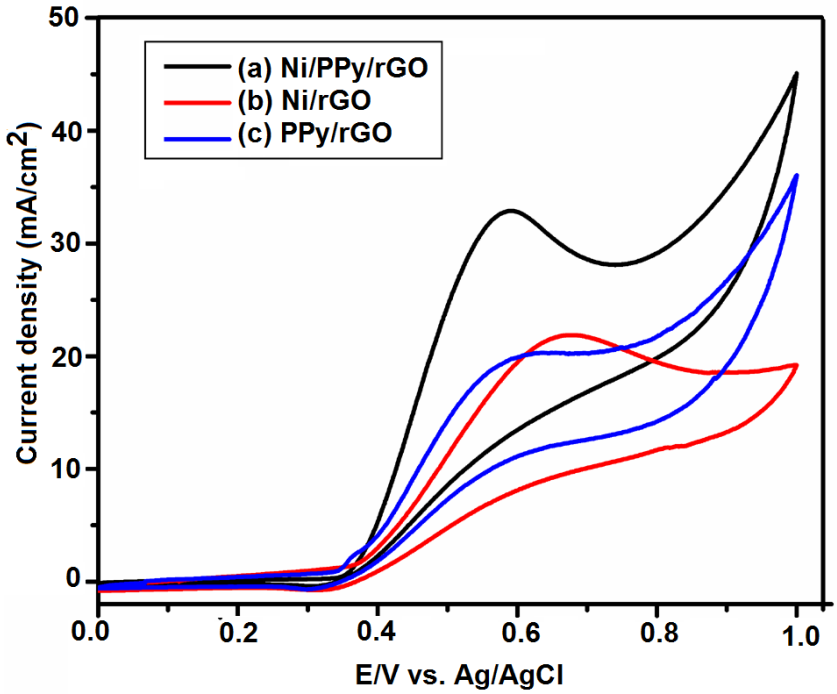

Fig. 3.13 CVs of the different composites (a) Ni/PPy/rGO, (b) Ni/rGO and (c) PPy/rGO in 1KOH + 1M methanol at 25°C and at the scan rate of 50 mVs^{-1} scan rate

The magnitude of the peak current density on the forward scan indicates the electrocatalytic activity of different electrocatalysts for methanol elcetro-oxidation. The anodic current density of the Ni/PPy/rGO is 32.94 mA/cm^2 which is higher than that of Ni/rGO (22.1 mA/cm^2) and PPy/rGO (20.35 mA/cm^2). Moreover, the onset potential of Ni/PPy/rGO is lower than that Ni/rGO and PPy/rGO. These results confirmed that Ni/PPy/rGO has the highest activity for methanol elctro-oxidation in alkaline medium. The greater electrochemical performance of Ni/PPy/rGO nanocomposites is due to the synergistic effect of Ni nanoparticles, rGO and PPy. The small size of Ni nanoparticles, uniform distribution of Ni nanoparticles over PPy/rGO surface with high surface area and conductivity and the utilization of the conducting polymer PPy to functionalized graphene which could provide high electrochemical surface area.

The durability of PPy/rGO, Ni/rGO and Ni/PPy/rGO were evaluated by chronoamperometry (Fig. 3.14) for 600s. During the first 50s, a slight decay in the current density was observed, which is due to the adsorption of intermediate products on the surface of the catalysts. After that, the current density reached a steady stable state throughout the entire period. The current density of the Ni/PPy/rGO nanocomposite was higher than that of PPy/rGO and Ni/rGO electrode. Thus, chronoamperometry study

reveals the superior durability, good tolerance against the intermediates and promising electro-catalytic activity of the nanocomposite for methanol oxidation.

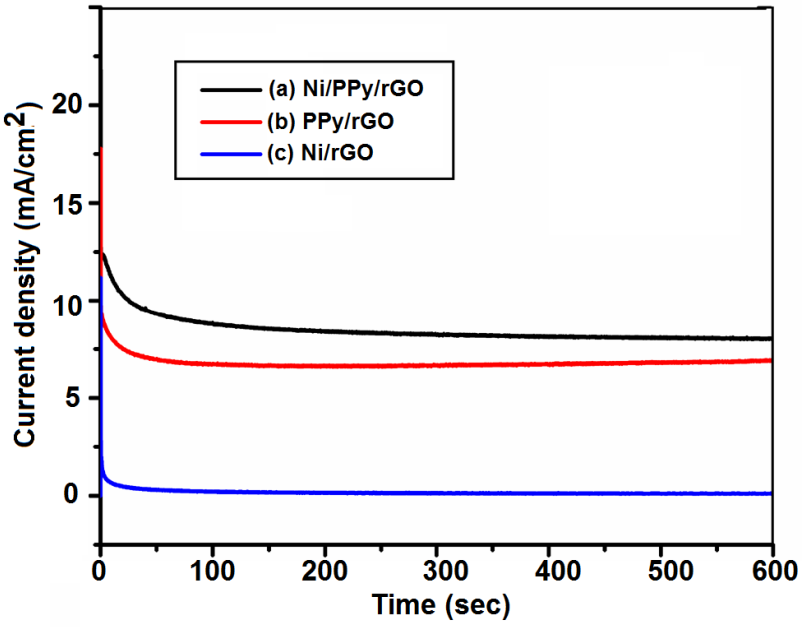

Fig. 3.14 Chronoamperograms of (a) Ni/PPy/rGO (b) Ni/rGO and (c) PPy/rGO in 1M KOH + 1M methanol at operational potential of 0.035V

3.4 Conclusion

A novel and simple synthetic approach has been reported for Ni nanoparticles supported on PPy/rGO surface and it can be used as multi-functional electrode in various applications. Characterization analysis showed that of Ni nanoparticles are uniformly distributed over rGO/PPy matrix. The Ni/PPy/rGO nanocomposite showed higher current density and superior CV area compared to rGO and PPy/rGO. Charging-discharging study revealed a high specific capacitance value (763.49 Fg^{-1}) of Ni/PPy/rGO nanocomposite at a current density 1.31 Ag^{-1} with capacity retention of 96.75 % after 200 cycles. Moreover, the Ni/PPy/rGO nanocomposite showed higher anodic current density and lower onset potential for methanol electro-oxidation. The improved electrochemical and electrocatalytical properties of Ni/PPy/rGO nanocomposites is due to the synergistic effect of Ni nanoparticles, rGO and PPy.

3.5 References

[1] Simon, P. and Gogotsi, Y. Materials for electrochemical capacitors. *In Nanoscience and Technology: A Collection of Reviews from Nature Journals,* 320-329, 2010.

[2] Yang, Z. and Nakashima, N. A simple preparation of very high methanol tolerant cathode electrocatalyst for direct methanol fuel cell based on polymer-coated carbon nanotube/platinum. *Scientific reports,* 5:12236, 2015.

[3] Winter, M. and Brodd, R. J. What Are Batteries, Fuel Cells, and Supercapacitors?. *Chemical reviews,* 105(3):1021-1021, 2005.

[4] Conway, B. E. *Electrochemical supercapacitors: scientific fundamentals and technological applications*. Klumer Academic/Plenum Publishers, New York, 1999.

[5] Dubal, D. P., Holze, R., and Gomez-Romero, P., Development of hybrid materials based on sponge supported reduced graphene oxide and transition metal hydroxides for hybrid energy storage devices. *Scientific reports,* 4:7349, 2014.

[6] Jafarian, M., Mahjani, M. G., Heli, H., Gobal, F., Khajehsharifi, H., and Hamedi, M. H. A study of the electro-catalytic oxidation of methanol on a cobalt hydroxide modified glassy carbon electrode. *Electrochimica Acta*, 48(23):3423-3429, 2003.

[7] Tiwari, J. N., Tiwari, R. N., Singh, G., and Kim, K. S. Recent progress in the development of cathode and anode catalysts for direct methanol fuel cells, *Nano Energy,* 2(5):553-578, 2013.

[8] Sarangapani, S., Tilak, B. V., and Chen, C. P. Materials for electrochemical capacitors theoretical and experimental constraints. *Journal of the Electrochemical Society,* 143(11):3791-3799, 1996.

[9] Liu, H., Wang, Y., Gou, X., Qi, T., Yang, J., and Ding, Y. Three-dimensional graphene/polyaniline composite material for high-performance supercapacitor applications. *Materials Science and Engineering: B,* 178(5):293-298, 2013.

[10] Xie, Y., Huang, C., Zhou, L., Liu, Y., and Huang, H. Supercapacitor application of nickel oxide–titania nanocomposites. *Composites Science and Technology*, 69(13):2108-2114, 2009.

[11] Chee, W. K., Lim, H. N., Zainal, Z., Huang, N. M., Harrison, I., and Andou, Y. Flexible graphene-based supercapacitors: a review. *The Journal of Physical Chemistry C,* 120(8):4153-4172, 2016.

[12] Subramanian, V., Zhu, H., and Wei, B. Synthesis and electrochemical characterizations of amorphous manganese oxide and single walled carbon nanotube composites as supercapacitor electrode materials. *Electrochemistry Communications,* 8(5):827-832, 2006.

[13] Zhu, J., Chen, M., Qu, H., Luo, Z., Wu, S., Colorado, H. A., Wei, S. and Guo, Z. Magnetic field induced capacitance enhancement in graphene and magnetic graphene nanocomposites. *Energy & Environmental Science,* 6(1):194-204, 2013.

[14] Rodriguez-Reinoso, F. The role of carbon materials in heterogeneous catalysis. *Carbon,* 36(3):159-175, 1998.

[15] Chen, C. Y., Chang, J. K., Tsai, W. T., and Hung, C. H. Uniform dispersion of Pd nanoparticles on carbon nanostructures using a supercritical fluid deposition technique and their catalytic performance towards hydrogen spillover. *Journal of Materials Chemistry*, 21(47):19063-19068, 2011.

[16] Steele, B. C. and Heinzel, A. Materials for fuel-cell technologies. *In Materials for Sustainable Energy: A Collection of Peer-Reviewed Research and Review Articles from Nature Publishing Group,* 224-231, 2011.

[17] Wang, S., Jiang, S. P., Wang, X., and Guo, J. Enhanced electrochemical activity of Pt nanowire network electrocatalysts for methanol oxidation reaction of fuel cells. *Electrochimica Acta*, 56(3):1563-1569, 2011.

[18] Zhao, X., Yin, M., Ma, L., Liang, L., Liu, C., Liao, J., Lu, T., and Xing, W. Recent advances in catalysts for direct methanol fuel cells. *Energy & Environmental Science*, 4(8):2736-2753, 2011.

[19] Zheng, W., Suominen, A., and Tuominen, A. Discussion on the challenges of DMFC catalyst loading process for mass production. *Energy Procedia,* 28:78-87, 2012.

[20] Brownson, D. A., Kampouris, D. K., and Banks, C. E. An overview of graphene in energy production and storage applications. *Journal of Power Sources,* 196(11):4873-4885, 2011.

[21] Stoller, M. D., Park, S., Zhu, Y., An, J., and Ruoff, R. S. Graphene-based ultracapacitors. *Nano letters,* 8(10):3498-3502, 2008.

[22] Yan, J., Wang, Q., Wei, T., Jiang, L., Zhang, M., Jing, X., and Fan, Z. Template-assisted low temperature synthesis of functionalized graphene for ultrahigh volumetric performance supercapacitors. *Acs Nano,* 8(5):4720-4729, 2014.

[23] Xia, X., Hao, Q., Lei, W., Wang, W., Sun, D., and Wang, X. Nanostructured ternary composites of graphene/Fe_2O_3/polyaniline for high-performance supercapacitors. *Journal of Materials Chemistry,* 22(33):16844-16850, 2012.

[24] Huang, H. and Wang, X. Recent progress on carbon-based support materials for electrocatalysts of direct methanol fuel cells. *Journal of Materials Chemistry A,* 2(18):6266-6291, 2014.

[25] Zhou, X., Qiao, J., Yang, L., and Zhang, J. A review of graphene-based nanostructural materials for both catalyst supports and metal-free catalysts in PEM fuel cell oxygen reduction reactions. *Advanced Energy Materials,* 4(8):1301523, 2014.

[26] Mahmood, N., Zhang, C., Yin, H., and Hou, Y. Graphene-based nanocomposites for energy storage and conversion in lithium batteries, supercapacitors and fuel cells. *Journal of Materials Chemistry A,* 2(1):15-32, 2014.

[27] Guo, S. and Dong, S. Graphene nanosheet: synthesis, molecular engineering, thin film, hybrids, and energy and analytical applications. *Chemical Society Reviews,* 40(5):2644-2672, 2011.

[28] Zhang, L., Shao, J. J., Zhang, W., Zhang, C., Zheng, X., Du, H., and Yang, Q. H., Graphene-based porous catalyst with high stability and activity for the methanol oxidation reaction. *The Journal of Physical Chemistry C,* 118(45):25918-25923, 2014.

[29] Novoselov, K. S. and Geim, A. K. The rise of graphene. *Nature Mater,* 6(3):183-191, 2007.

[30] Huang, X., Li, S., Huang, Y., Wu, S., Zhou, X., Li, S., Gan, C. L., Boey, F., Mirkin, C. A., and Zhang, H. Synthesis of hexagonal close-packed gold nanostructures. *Nature communications,* 2:292, 2011.

[31] Zhang, Y., Li, H., Pan, L., Lu, T., and Sun, Z. Capacitive behavior of graphene–ZnO composite film for supercapacitors. *Journal of Electroanalytical Chemistry,* 634(1):68-71, 2009.

[32] Wang, H., Casalongue, H. S., Liang, Y. and Dai, H. $Ni(OH)_2$ nanoplates grown on graphene as advanced electrochemical pseudocapacitor materials. *Journal of the American Chemical Society,* 132(21):7472-7477, 2010.

[33] Zhang, K., Zhang, L. L., Zhao, X. S., and Wu, J. Graphene/polyaniline nanofiber composites as supercapacitor electrodes. *Chemistry of Materials*, 22(4):1392-1401, 2010.

[34] Zaid, N. A. M. and Idris, N. H. Enhanced capacitance of hybrid layered graphene/nickel nanocomposite for supercapacitors. *Scientific reports*, 6:32082, 2016.

[35] Zhang, L. R., Zhao, J., Li, M., Ni, H. T., Zhang, J. L., Feng, X. M., Ma, Y. W., Fan, Q. L., Wang, X. Z., Hu, Z., and Huang, W. Preparation of graphene supported nickel nanoparticles and their application to methanol electrooxidation in alkaline medium. *New Journal of Chemistry*, 36(4)-1108-1113, 2012.

[36] Zhao, H., Li, L., Yang, J., Zhang, Y., and Li, H. Synthesis and characterization of bimetallic Pt–Fe/polypyrrole–carbon catalyst as DMFC anode catalyst. *Electrochemistry Communications*, 10(6):876-879, 2008.

[37] Zhao, H., Li, L., Yang, J., and Zhang, Y. Nanostructured polypyrrole/carbon composite as Pt catalyst support for fuel cell applications. *Journal of Power Sources*, 184(2):375-380, 2008.

[38] William, S., Hummers, Jr. and Offeman, R. E., Preparation of graphitic oxide. *Journal of the American Chemical Society*, 80(6):1339-1339, 1958.

[39] Bora, C. and Dolui, S. K. Interfacial synthesis of polypyrrole/graphene composites and investigation of their optical, electrical and electrochemical properties. *Polymer International*, 63(8):1439-1446, 2014.

[40] Sahoo, S., Karthikeyan, G., Nayak, G. C., and Das, C. K. Electrochemical characterization of in situ polypyrrole coated graphene nanocomposites. *Synthetic Metals*, 161(15-16):1713-1719, 2011.

[41] Chang, H. H., Chang, C. K., Tsai, Y. C., and Liao, C. S. Electrochemically synthesized graphene/polypyrrole composites and their use in supercapacitor. *Carbon*, 50(6):2331-2336, 2012.

[42] Zhang, L. L., Zhao, S., Tian, X. N. and Zhao, X. S. Layered graphene oxide nanostructures with sandwiched conducting polymers as supercapacitor electrodes. *Langmuir*, 26(22):17624-17628, 2010.

[43] Senthamilselvan, D., Chezhian, A., Kabilan, N., Kumar, S. T., and Kumaran, S. N. FTIR study of Nickel and Mercury induced biochemical changes in the muscles

tissues of Lates Calcarifer. *International Journal of Environmental Sciences*, 2(4):1976, 2012.

[44] Sahoo, N. G., Jung, Y. C., So, H. H., and Cho, J. W. Polypyrrole coated carbon nanotubes: Synthesis, characterization, and enhanced electrical properties. *Synthetic Metals*, 157(8-9):374-379, 2007.

[45] Duchet, J., Legras, R., and Demoustier-Champagne, S. Chemical synthesis of polypyrrole: structure–properties relationship. *Synthetic metals*, 98(2):113-122, 1998.

[46] Furukawa, Y., Tazawa, S., Fujii, Y., and Harada, I. Raman spectra of polypyrrole and its 2, 5-13C-substituted and C-deuterated analogues in doped and undoped states, *Synthetic metals*, 24(4):329-34, 1988.

[47] Robertson, P. M. On the oxidation of alcohols and amines at nickel oxide electrodes: mechanistic aspects. *Journal of Electroanalytical Chemistry and Interfacial Electrochemistry*, 111(1):97-104, 1980.

[48] Taraszewska, J. and Rosłonek, G. Electrocatalytic oxidation of methanol on a glassy carbon electrode modified by nickel hydroxide formed by ex situ chemical precipitation. *Journal of Electroanalytical Chemistry*, 364(1-2):209-213, 1994.

[49] Yang, J., Zhang, E., Li, X., Yu, Y., Qu, J., and Yu, Z. Z. Direct reduction of graphene oxide by Ni foam as a high-capacitance supercapacitor electrode. *ACS applied materials & interfaces*, 8(3):2297-2305, 2016.

[50] Fleischmann, M., Korinek, K., and Pletcher, D. The oxidation of organic compounds at a nickel anode in alkaline solution. *Journal of Electroanalytical Chemistry and Interfacial Electrochemistry*, 31(1):39-49, 1971.

[51] Fleischmann, M., Korinek, K., and Pletcher, D. The kinetics and mechanism of the oxidation of amines and alcohols at oxide-covered nickel, silver, copper, and cobalt electrodes. *Journal of the Chemical Society, Perkin Transactions* 2(10):1396-1403, 1972.